




# Scaling laws for the water entry of a three-dimensional body

Cite as: Phys. Fluids **33**, 036104 (2021); <https://doi.org/10.1063/5.0038210>

Submitted: 20 November 2020 • Accepted: 26 January 2021 • Published Online: 04 March 2021

 Claudio Lugni,  Jingbo Wang (王经博),  Odd Magnus Faltinsen, et al.

## COLLECTIONS

 This paper was selected as an Editor's Pick



View Online



Export Citation



CrossMark

## ARTICLES YOU MAY BE INTERESTED IN

[Experimental study of the effects of a viscous liquid layer on the cavity dynamics of vertical entry by a sphere into water at low Froude number](#)

Phys. Fluids **33**, 013308 (2021); <https://doi.org/10.1063/5.0032818>

[Dynamics of the cavity evolution during vertical water entry of deformable spheres](#)

Phys. Fluids **33**, 065106 (2021); <https://doi.org/10.1063/5.0051401>

[A hybrid model for simulation of fluid–structure interaction in water entry problems](#)

Phys. Fluids **33**, 017102 (2021); <https://doi.org/10.1063/5.0031681>

APL Machine Learning

Open, quality research for the networking communities

MEET OUR NEW EDITOR-IN-CHIEF

LEARN MORE



# Scaling laws for the water entry of a three-dimensional body

Cite as: Phys. Fluids **33**, 036104 (2021); doi: [10.1063/5.0038210](https://doi.org/10.1063/5.0038210)

Submitted: 20 November 2020 · Accepted: 26 January 2021 ·

Published Online: 4 March 2021



View Online



Export Citation



CrossMark

Claudio Lugni,<sup>1,2,3,a)</sup>  Jingbo Wang (王经博),<sup>1,a)</sup>  Odd Magnus Faltinsen,<sup>3</sup>  Andrea Bardazzi,<sup>2,4</sup> Alessia Lucarelli,<sup>2</sup> and Wenyang Duan (段文洋)<sup>1</sup>

## AFFILIATIONS

<sup>1</sup>Institute of Marine Hydrodynamics, Harbin Engineering University, Harbin, China

<sup>2</sup>CNR-INM, Marine Technology Research Institute, Via di Vallerano 139, 00128 Roma, Italy

<sup>3</sup>NTNU-AMOS, Center for Autonomous Marine Operation Systems, Otto Nielsens vei 10, N-7491 Trondheim, Norway

<sup>4</sup>Università degli Studi della Campania 'Luigi Vanvitelli', Via Roma 29-81031 Aversa (CE), Italy

<sup>a)</sup> Authors to whom correspondence should be addressed: [claudio.lugni@cnr.it](mailto:claudio.lugni@cnr.it) and [jingbowang@hrbeu.edu.cn](mailto:jingbowang@hrbeu.edu.cn)

## ABSTRACT

The present experimental investigation is a new way of conducting tests on model scale and of interpreting the results for the water entry of a free-falling conical body shape entrapping an air cavity. A three-dimensional body free to fall from different heights against a flat water surface is studied. Accurate measurements of the acceleration and velocity in water are performed; for the first time, local measurements of the pressure field in the air cavity entrapped behind the falling body are executed. The use of a depressurized channel enabled the scaling of the local loads as a function of Froude and Euler numbers. In spite of their uniqueness, the present results refer to one specific body shape and one specific mass-ratio value. Other similar studies are needed for a full comprehension of the universality of the scaling law for this physical phenomenon. The availability of such an experimental analysis enables a proper validation of the numerical models that can be, then, used for more general studies.

Published under license by AIP Publishing. <https://doi.org/10.1063/5.0038210>

## I. INTRODUCTION

The water entry of a body is of interest in several marine applications, from the slamming of ship bows<sup>1</sup> or the launch of life boats<sup>2,3</sup> up to the projectile<sup>4</sup> and missile<sup>5</sup> entering the water for military purposes or solid objects unexpectedly falling into the sea as a consequence of a marine operation failure.<sup>6</sup> More recently, it also received attention for the common hydrodynamic features with bio-inspired water walking creatures.<sup>7</sup>

The problem is complex from the physical point of view because it involves several challenging phenomena common to marine flows, from the impulsive loads during the slamming stage up to the multi-phase flows in the jet and the cavity evolution behind the body. For the water-entry problem of a solid body with density  $\rho_s$  and characteristic length  $c_0$  (e.g., the maximum radius of an axisymmetric body) falling through a gas (with density  $\rho_g$  and ullage pressure  $p_u$ ) and impacting a calm liquid (with density  $\rho$ , kinematic viscosity  $\nu$ , surface tension  $\sigma$ , and vapor pressure  $p_v$ ) surface at a velocity  $U_0$ , the Pi theorem enables the definition of the following dimensionless groups:

- Reynolds number  $Re = U_0 c_0 / \nu$ , giving the balance between inertial and viscous forces;
- Weber number  $We = \rho U_0^2 c_0 / \sigma$  for the balance between inertial and capillary forces;
- $Fn = U_0 / \sqrt{g c_0}$  expressing the balance between inertial and gravitational forces,
- cavitation number  $Cn = (p - p_v) / (0.5 \rho U_0^2)$  with  $p$  the local pressure in the fluid, giving the balance between cavitation and inertial forces;
- Euler number  $Eu = p_u / (0.5 \rho U_0^2)$  meaning the balance between gas compressibility and body inertia;
- solid/liquid density ratio  $D = \rho_s / \rho$ , directly related to the body mass and liquid added mass, which may express the balance between the body inertia and added-mass forces; and
- gas/liquid density ratio  $\tilde{D} = \rho_g / \rho$ .

Note that from these nondimensional groups, others may be defined; they are capillary number  $Ca = We/Re = \rho \nu U_0 / \sigma$ , which gives the balance between viscous and capillary contributions and

Bond number  $Bo = We/Fn^2 = \rho g c_0^2 / \sigma$ , related to the balance between gravity and capillary forces.

Experimental observations by Aristoff *et al.*<sup>8</sup> assessed the occurrence of different types of air-entrained cavities behind a free fall sphere during the water entry at  $Re \gg 1$ ,  $Cn \gg 1$ ,  $D > 1$  and  $\tilde{D} = 1.2 \times 10^{-3}$ . They were related to the balance among inertial, capillary, and gravitational forces, through Bond and Froude numbers. In the flow regime  $Bo > 10$ , they reported three different types of cavity closures, which depend on  $Fn$ . At really low  $Fn$ , a tiny bubble is entrapped on or near the body at the cavity pinch-off: this is the *quasi-static* seal type, which characterizes the cavity behind the falling body when it is almost unable to fully penetrate the free surface because of the large contribution of the capillary force, i.e., for  $We \ll 1$ . By increasing the impact speed, the second type of cavity closure is observed for  $Fn < 10$ : the *deep seal* that occurs above the body and below the undisturbed free surface as a consequence of the gravitational effects, more specifically, of the hydrostatic forces counteracting the inertia terms. Two opposite jets arise at the pinch-off: the Worthington jet, directed upward, and the other moving down and impacting with the top part of the body, possibly modifying its trajectory. For slender bodies, e.g., projectiles, the cavity closure occurs first on the side of the body.

Still increasing  $Fn$  above 10, corresponding to the large  $We$ , the fluid inertia dominates and contrasts the collapse tendency of the cavity due to gravity, developing an elongated cavity; the pinch-off point moves up until the undisturbed liquid surface level, realizing the third type of closure: the *surface seal*. Similar to the deep-seal type, two opposite jets are formed; however, because of the elongated cavity, the downward jet has smaller effects on the body trajectory.

Concerning the role of the cavitation number, a detailed study was done by Gilbarg and Anderson<sup>9</sup> on a sphere impacting a still water surface at large speed ( $Fn > 12$ ). The authors were interested in the cavity seal type, concluding that the sealing type can change from the deep to the surface seal type depending on the cavitation number. However, no load measurements were done.

Our investigation focuses on the evolution of the air cavity behind a axisymmetric conical body shape impacting the water surface at relatively low Froude numbers, namely,  $Fn < 4$ , at  $Re > 10^5$ ,  $D > 1$ ,  $We \gg 1$ , and  $Bo \gg 1$ ; under these conditions, an air-entraining deep-seal cavity is observed.

All the above experimental studies focused on the first stages of the water entry, namely, until the pinch-off event. However, to our knowledge, no experimental investigation exists on the post-closure cavity evolution and on the scaling problem of the cavity dynamics-induced loads on the body. These are the main objectives of the present research activity.

For the first time, a systematic investigation has been carried out to study the repercussion of the ullage pressure, through the Euler number, on the cavity dynamics after the closure, governed by the coupled body-cavity resonance: the external hydrodynamics, Froude dominated, coercing the cavity to implode, is counteracted by the action of the air compressibility, strongly influenced by the Euler number. The scaling of the local loads in the cavity with  $Eu$  and its possible effects on the body motion are here experimentally assessed.

## II. METHODS: EXPERIMENTAL SETUP

Figure 1 shows a global sketch of the setup designed specifically for this experiment.

The depressurized channel facility available at INM [panel (i) in Fig. 1] has been used; it has a transverse section in the test area of  $3.6 \text{ m} \times 3 \text{ m}$  ( $W \times H$ ) and operates with a water depth of 2.25 m. In order to increase the maximum falling height of the cone, for a higher initial impact velocity  $V = \sqrt{2gH_f}$ , (with  $H_f$  the free fall height), a prismatic steel dome [panels (ii) and (iii) in Fig. 1] has been properly designed and built on the stainless steel lid of the depressurized tank. The dome is composed of a cylindrical tube and a rectangular box [panel (iii) in Fig. 1]; it cannot be larger than the distance between two transverse stiffeners of the channel lid, providing then a limit to the value of the cone radius, which has been chosen as  $c_0 = 125 \text{ mm}$ .

In the dome, a pulley system with an external handwheel [panels (ii) and (iii) in Fig. 1] is realized to recover and lift up the cone at the end of each test, through the wire  $d$  [panel (ii) Fig. 1] connected to the center of the cone. Three vertical steel wires [ $a$ ,  $b$ , and  $c$ , panel (ii) in Fig. 1] connected to the fixed part of the dome (on the top) and at the bottom of the channel have been used to guide the vertical trajectory of the body during the falling and restrain its possible rotation. For this purpose, the three wires pass through three holes on the body such that the body slides on the wires during the fall. While the frictional contribution of the latters can be neglected, the pulley system showed some frictional effects that are not negligible, in particular during the fall of the cone in air. During this stage, in fact, the wire sliding on the pulley gives friction because of the bearings used to connect the internal pulley with the external handwheel. An accurate sealing has been ensured to reduce as much as possible the air leakage during the test in depressurized conditions. This constraint is in conflict with the small friction requirement, and a compromise must be found. For the present case, the depressurized channel has the standard leakage of 7–8 mbar per minute at the lowest pressure condition, which ensures a fully negligible effect of the leakage for the used sealing system.

During the fall in air, the cone is undergone to gravity force, aerodynamic drag (assumed negligible), mechanical friction at the handwheel, and tension of the cables  $d$  connected to the body. The latter can induce some oscillations in the vertical acceleration of the body before the impact, around a mean value, which is lower than  $g$ , causing a reduction of the velocity of the body at the impact time with respect to the ideal value  $V = \sqrt{2gH_f}$ . For these reasons, the correct value of the impact velocity and of the body trajectory has been accurately measured, through both the integration of the accelerometer and the image analysis, ensuring a maximum error of  $\pm 1 \text{ mm}$  for the vertical displacement and  $\pm 1 \text{ mm/s}$  for the velocity of the body.

After the body enters the water surface, the large impact force<sup>2,10,11</sup> makes the effects related to the handwheel friction and cable tension completely negligible since the cable quickly becomes slack. Particular care has been dedicated to the design of the body. Realized from a single aluminum block, properly emptied through a milling machine, it is composed of a cone with a radius  $c_0$  and a height of 125 mm so to get a deadrise angle of  $45^\circ$  and a cylindrical body with the same radius  $c_0$  and a height of 65 mm (left panel of Fig. 2). The cylindrical body was necessary to host the home-made wireless DAQ system along with the battery pack, used to power the DAQ, the transducers, and the bluetooth transfer device. Close to the apex of the cone, suitable melted lead weights were used to catch the target total weight of the body and minimize the space for the ballast. To get a complete monitoring of the body motions and the local loads on the body, the cone was equipped with

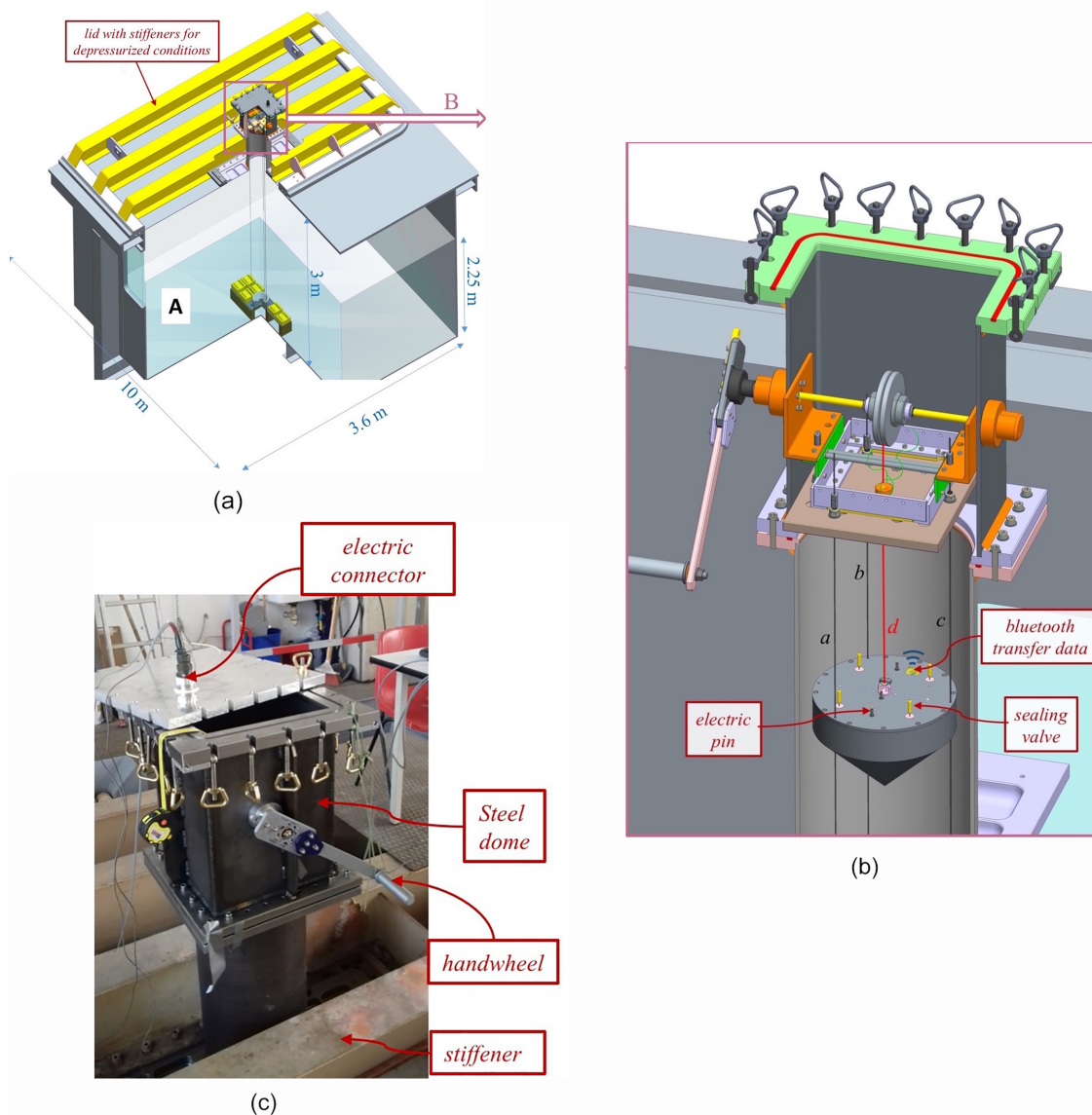


FIG. 1. (i) Sketch of the INM depressurized channel, (ii) internal view of the dome with the setup used, and (iii) dome realized on the channel lid.

- one MEMS tri-axis accelerometer SDI 2422H low voltage 5VDC with a full range of  $\pm 5$  g;
- an electromagnetic trigger to synchronize the body measurements with the digital fast cameras and the hydrophones in the channel;
- seven micro differential pressure transducers (Helm H91) with a Full Scale (FS) 50 kPa, an overall accuracy of 0.1% FS, and a natural frequency in air of 200 kHz have been used. More in detail, (i) three pressure sensors along the impact side of the cone, namely,  $P_{s_1}$ ,  $P_{s_2}$ , and  $P_{s_3}$  (left panel of Fig. 3); the first two are positioned at a distance of 82 mm and 122 mm from the cone

apex along the apothem, and the third one is positioned on the symmetric apothem of the cone, at the same distance of  $P_{s_2}$ ; (ii) four sensors on the body lid, at the position indicated on the right panel of Fig. 3.

To guarantee the same pressure between the external part of the body, i.e., the ullage pressure of the depressurized channel, and the internal part of the body, essential for the accurate measurement of differential pressure transducers, four mechanical valves were designed and realized at INM and installed on the cone cover (sealing valve in Fig. 2). They are open when the body is in the initial position and

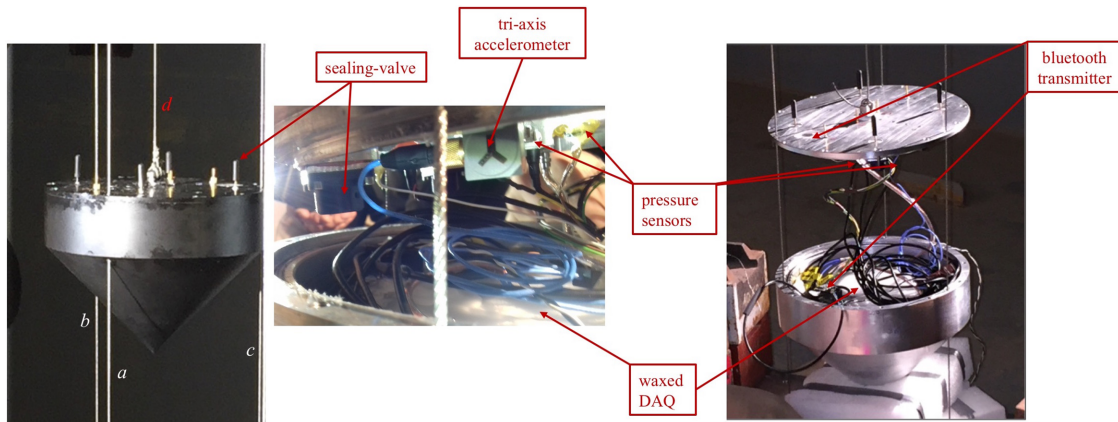


FIG. 2. Close view of the body.

closed during each run. Finally, four electric pins are mounted on the cone to enable the recharge of the internal battery during the waiting time between two runs. They are connected to the external electrical power through the connector mounted on the cover of the dome.

Two fast speed cameras (PHOTRON Mini AX-100) are used to ensure an accurate view of the full evolution of the body and reduce the lens aberration on the boundary of the images. To this aim, the two fields of the cameras are reconstructed so to remove the boundaries. The camera frames are synchronized with the signals recorded by the DAQ in the body through an electromagnetic trigger system suitably designed. The cameras recorded with a resolution of  $1024 \times 1024$  at 2000 frames per second. Particular care has been dedicated to the measure of the ullage pressure in the tank, which is relevant for the Euler number estimation. Two different pressure transducers, placed on the lateral wall and above the calm water level of the tank, at a distance of approximately 4 and 8 m, respectively, from the cone model, constitute the customized monitoring system used in the depressurized circulating channel at CNR-INM. They are periodically calibrated during the year and, in any case, at the beginning and at the end of the present experiments, showing a linearity

error within 0.3%. The digital value (reading accuracy: 0.1 mbar) from the two pressure transducers during each test (duration: less than 1 s) has been recorded by two different operators and memorized in the test matrix. The leakage of the depressurized facility is extremely low and, at the lowest ullage pressure, limited to 7–8 mbar per minute. Typically, for tests with long duration, the operator activates the empty pump system to keep the pressure constant. However, within the short duration of the present test, this system has been not activated, in order to avoid transient effects.

**A. Uncertainty analysis**

Almost all the results related to the quantities measured in Sec. III are complemented with an error bar, which gives a global estimation of the maximum expected error. Only the repeatability error is estimated, with the bias error being omitted in the present analysis; however, possible bias error sources will be discussed later. An accurate estimation of the repeatability error requires the repetition of the same test several times, which is time consuming and inconceivable to be performed for each test condition. In the present experiments, each

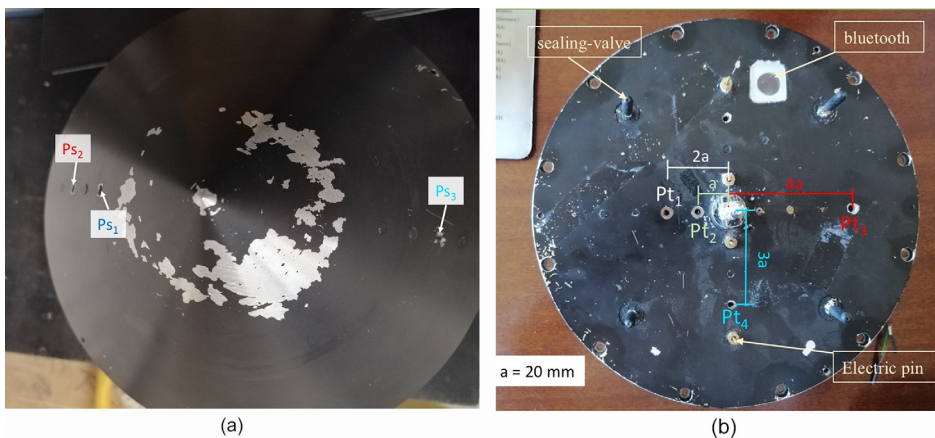


FIG. 3. Position of the pressure transducers on the cone.

test condition has been repeated at least  $N=3$  times; this is definitely not sufficient to get a proper error estimation, but it is a good way to check the repeatability. However, since the runs at the same Froude numbers ( $Fn$ ) have been repeated for several ullage pressures, we can definitely get a good estimation of the repeatability error for the physical quantities before the pinch-off instant and at the same  $Fn$ ; in this case, in fact,  $N \gg 3$ , and no dependence on the Euler number ( $Eu$ ) can be assumed. This allows for the calculation of the mean quantity  $\bar{q}$

$$\bar{q} = \frac{1}{N} \sum_{i=1}^N q_i$$

and of the associated standard deviation

$$S_q = \sqrt{\frac{1}{N-1} \sum_{i=1}^N (q_i - \bar{q})^2}.$$

It is important to stress the validity of the above estimation only before the cavity closure, for which the different used ullage pressure conditions do not influence the measured value, and then,  $N > 3$  can be assumed. In contrast, for the quantities measured after the cavity closure, the error bar corresponding to the standard deviation is only given for the cases where at least  $N=4$  repeated tests have been performed. Alternatively, for the quantities related to the pressure within the cavity, the error bar has been calculated by considering the signals from the four pressure transducers in the cavity. It is finally worth to say that all the repeated tests have been done without repeating the image recordings using the fast cameras. This is related to the huge amount of data required by the camera recordings. For this reason, almost all the quantities estimated from the camera images do not show any error bar (Figs. 9–12), except for the volume and the geometry of the cavity just before the cavity closure (Figs. 6 and 7), for which we assumed no dependence on the  $Eu$  number, as done for the previous quantities. However, for the cases where no error bar is provided, we can give here an estimation of the error based on the analysis procedure done. In fact, it is reasonable to assume an error on the definition of the geometrical quantities by the images about 1–2 pixels, which corresponds to 1–2 mm. This means an error referred to the radius  $c_0$  of the cone (used to get the dimensionless geometrical quantities reported in Figs. 9–12) approximately equal to 1%–2%. Although this value is small with respect to the mean value reported in the figures, it can become relevant when the velocity is calculated, as in the right panel of Fig. 9, because of the small time interval considered. To appreciate a variation in the measurement of the radial distance of the neck during the time evolution of the cavity closure, a time interval of at least 2 ms has been chosen (i.e., 4 images). This implies an error in the estimation of the nondimensional velocity reported in the right panel of Fig. 9, approximately equal to 0.7–0.8, which corresponds to 50% for the lowest value of the nondimensional velocity and to 10% for the largest one.

The estimation of the bias error sources is more challenging. In our experimental setup, we have identified the following possible error sources:

- friction of the wire during the free-falling stage of the cone,
- air leakage from the channel,

- effect of the wire on the cavity closure and jet development, and
- cone-channel side or bottom interference.

In the setup description, we have already discussed the first two error sources, and we have definitely assessed that their role can be assumed small. In particular, the first one could matter during the cone free-falling in air becomes definitely negligible after the impact. For this reason, we have measured in two different ways (i.e., through images and accelerometers) the velocity of the body at the impact time instant, and we have estimated the corresponding  $Fn$  standard deviation achieved from repeated tests according to the above description of the error. This means that the error bar shown for  $Fn$  takes into account also this error source. Concerning the air leakage, we have assessed its minor role during the short time of the test. The possible effect of the wire on the cavity closure and on the downward and upward jet development is not easy to be established. Because of the wire thickness (radius 1 mm) and the horizontal velocity (larger than 2.5 m/s) of the incoming water flow, we can guess a minor role in the cavity closure; if a variation of the time instant corresponding to the full cavity closure can be expected, this should be comparable to  $1/2500 \approx 0.4$  ms, i.e., within the uncertainty of the time resolution of the camera. A similar effect can be expected on the formation of the upward and downward jets. However, in this case, some local effects due to surface tension along the wire can be expected, which could slightly modify the velocity of the jet, possibly causing its slowdown. Finally, the interference of the cone pressure field with the tank wall requires a more detailed analysis. In principle, we can identify two possible physical mechanisms: free-surface wave generation due to the body entering into the water and acoustic waves generated at the impact and cavity closure time instants. Because of the lateral size of the cone ( $c_0 = 125$  mm) with respect to the shortest half size of the channel ( $W = 1800$  mm) and the short time of the test (0.4 s), the free-surface waves are definitely negligible. By using, indeed, a really over-estimated wave velocity, based on shallow water approximation, we get  $\sqrt{gh} \approx 4.6$  m/s, with  $h = 2.25$  m. This means that the effect of the wave reflection by the wall occurs after 760 ms, i.e., well after the end of the test. We can question on the reflection of the acoustic wave in the water, possibly generated during the impact of the cone on the calm free surface and the liquid-liquid impact at the closure of the cavity. Concerning the body impact stage, according to Korobkin and Peregrine,<sup>12</sup> the supersonic stage in the water matters for a Mach number of  $\approx \mathcal{O}(1)$ . In the present experiments, the Mach number is defined as the ratio between the impact velocity normal to the body surface, i.e.,  $V/\tan \delta$ , with  $\delta$  the deadrise angle of the cone, and the speed of sound in water. This implies  $M \approx \mathcal{O}(10^{-4}) \ll 1$ , that is, acoustic effects are negligible. When the cavity closes, a liquid-liquid impact occurs. A similar analysis states that the acoustic effects due to the liquid-liquid impact are negligible. Finally, when the cavity oscillates, there will be acoustic effects in the liquid when the frequency of oscillation is very high,<sup>13,14</sup> which is not the case of our experiments. Based on these considerations, we can assess that the acoustic effects can be completely neglected in our experiments.

### III. RESULTS AND DISCUSSION

Our analysis refers to the experimental results of a free fall vertical axisymmetric body with density ratio  $D = 1.88$ , which impacts a still water surface at a velocity  $U_0$ . The body is composed of a cone with radius  $c_0 = 125$  mm and a deadrise angle of  $45^\circ$  and a closed

cylinder of radius  $c_0$  and height  $h = 65$  mm. The mass ratio is defined as  $D^* = m/m_{ref}$ , where  $m$  is the mass of the body and  $m_{ref} = 4/3\rho c_0^3$  is proportional to the liquid added mass of the body; in the present experiments,  $D^* = 3.78$ . Four different Froude numbers, namely,  $Fn = 1.64, 2.45, 3.16,$  and  $3.98$ , are considered; in order to investigate the Eu-scaling effect, five different ullage pressure values, from atmospheric down to 42 mbar, have been investigated; this combination allows an  $Eu$  variation from 0.5 up to 60. For the examined conditions,  $Bo \approx 2100$ ,  $We > 5700$ , and  $Re > 2 \times 10^5$  ensure a negligible role of the surface tension and viscosity with respect to the inertial and gravitational forces, at least until the closure of the cavity, and to the compressibility terms after the closure. The measurements of the pressure along the cone and on the top part of the cylinder, i.e., within the cavity, and of the vertical acceleration of the body and the images of two high-speed cameras (section Methods for further details) will corroborate the discussion of the following results.

### A. Flow evolution until the closure of the cavity

With the aim to provide a global picture of the scenario, from the initial impact (at  $t = t_A$ ) until the cavity closure (at  $t = t_H$ ), we refer to the results of the experimental test conditions ( $p_u = p_{atm}$  and  $Fn = 3.98$ ) reported in Fig. 4. For the body shape here considered, the impulsive hydrodynamic forces during the impact cause a quick deceleration of the body with an evident spray, which arises in correspondence of the flow detachment (time  $t_C$  in Fig. 4) at the end of the conical body: the time rate of change of liquid momentum related to the time variation of the high-frequency vertical added mass term induced by the quick variation of the wetted body surface dominates<sup>1,15</sup> the body dynamics at this stage. The peak pressure, moving at the constant jet root speed, is recorded using two pressure transducers vertically positioned along the body ( $Ps_1$  and  $Ps_2$  in Fig. 4). The third pressure transducer  $Ps_3$ , placed at the same vertical coordinate of  $Ps_2$  but at the opposite radial position, confirms the axisymmetry of the problem. Successively, cavity creation occurs.<sup>4</sup>

According to Truscott *et al.*,<sup>4</sup> two different physical mechanisms govern the cavity creation: air entrainment or cavitation. The former is the typical phenomenon that occurs at a relatively low impact velocity behind a bluff body;<sup>16</sup> it is, then, characterized by  $Cn \gg 1$  and  $Fn \geq 1$ . The cavitation mechanism characterizes the cavity formation at high velocity of the body, which gives rise to extremely low local fluid pressure (i.e., close to the vapor pressure), with liquid vaporization, i.e.,  $Cn < 1$  and  $Fn \gg 1$ ; the cavity can be filled with an air-steam mixture. In some circumstances, i.e.,  $Cn \leq 0$ , a vapor cloud embeds the whole body, developing a supercavitating flow with potential positive consequences on the drag reduction.<sup>17</sup> In our experiments, the air-entrainment type is always observed, independent of the ullage pressure considered; this is probably related to the relatively low impact speed examined, i.e.,  $Fn < 4$ . The scenario of the cavity formation is still illustrated in Fig. 4, from  $t_C$  up to the closure time instant at  $t = t_H$ . For similar conditions, within the potential-flow assumption, a detailed analysis of the force contribution affected by the open cavity behind axisymmetric bodies (two-dimensional, i.e., 2D, and three-dimensional, i.e., 3D, with different shapes) is proposed in Wang *et al.*<sup>10</sup> and will be here used to interpret the experimental findings.

At  $t = t_C$ , the jet flow leaves the cone end tangentially; the velocity-force term,<sup>10</sup> related to the body velocity and to the liquid velocity field, governs the body dynamics (and then, the acceleration

of the body), when the upper part of the solid is still near the undisturbed free surface, with a small contribution from the acceleration-force term, related to the vertical free-surface dependent added mass of the fully wetted cone and to the gravity-force term. When the depth of the body increases ( $t_D$ ,  $t_E$ , and  $t_F$ ), the decreasing velocity-force term is counteracted by the increasing gravity-force term, sum of the hydrostatic (increasing with the body depth) and dynamic g-terms (also increasing with the body depth but at a smaller rate with respect to the hydrostatic term<sup>10</sup>). After  $t = t_F$ , the gravitational terms dominate the hydrodynamic forces on the body until the cavity pinch-off occurring at  $t_p \approx t_H$ ; the acceleration term assumes a minor role. Note that hereinafter  $t_H$  indicates the time instant of the experimental image closest to the pinch-off time  $t_p$ , within the time resolution of the camera used (i.e.,  $dt = 0.5$  ms). It is interesting that both the local (i.e., pressure on the body) and global loads (i.e., body acceleration) around  $t = t_C$  (enlarged view of the rectangular windows highlighted in Fig. 4) show a local increase around that time instant. This is related to the closure of a local cavity at the lateral side of the cylindrical extension of the body, above the cone: the small cavity, more similar to an air layer, squeezing from top to bottom, is suddenly wiped away by the massive water body around. This induces a sudden variation of the added mass and then an increase in the vertical force. The squeezing of the cavity on the cylindrical part of the body is counteracted by the compressibility effects of the air in the cavity layer, which opposes to its contraction. As a consequence, this force contribution is expected to depend on the ullage pressure of the air in the tank. However, the experimental observation shows that this local phenomenon does not influence the closure of the main cavity behind the body, dominated by the gravitational and inertial effects of the closing water mass.

Since the aim of the present research investigation is the scaling of the main physical parameters involved in the water-entry problem of an axisymmetric body, it is interesting to inspect the geometrical and kinematic quantities characterizing the cavity at the pinch-off moment.

At the pinch-off time instant, instead, a first closed air-cavity is generated above the body and moves with it, while a second open cavity, bounded by the original free surface, moves in the opposite direction to fill the air portion left by the body impact. Figure 5 shows the experimental image of the two cavities just before the closure time instant and for different Froude numbers, varying from 1.64 up to 3.98. The white circle indicates the position of the pinch-off point, which separates the two cavities. Its distance from the undisturbed free-surface,  $z_p$ , is represented by the cyan line in Fig. 5 and along with the angle  $\beta$  provides a measure of the axisymmetric open cavity volume, as well as of its slenderness. Similarly, the distance  $h$  between the pinch-off point and the center of the aft-body (red line) represents the height of the closed cavity and provides, along with the angle  $\alpha$ , a measure of the slenderness of the axisymmetric closed air cavity. For the latter, the volume of the cavity has also been estimated by assuming the axisymmetric shape of the cavity,

$$Vol = \pi \int_0^h f^2(z - (h + z_p)) dz, \quad (1)$$

with  $f(z)$  the external boundary of the shaded area in Fig. 5 (black line).

A first visual inspection confirms that the geometry of the cavity depends on the impact velocity, i.e., through the Froude number.

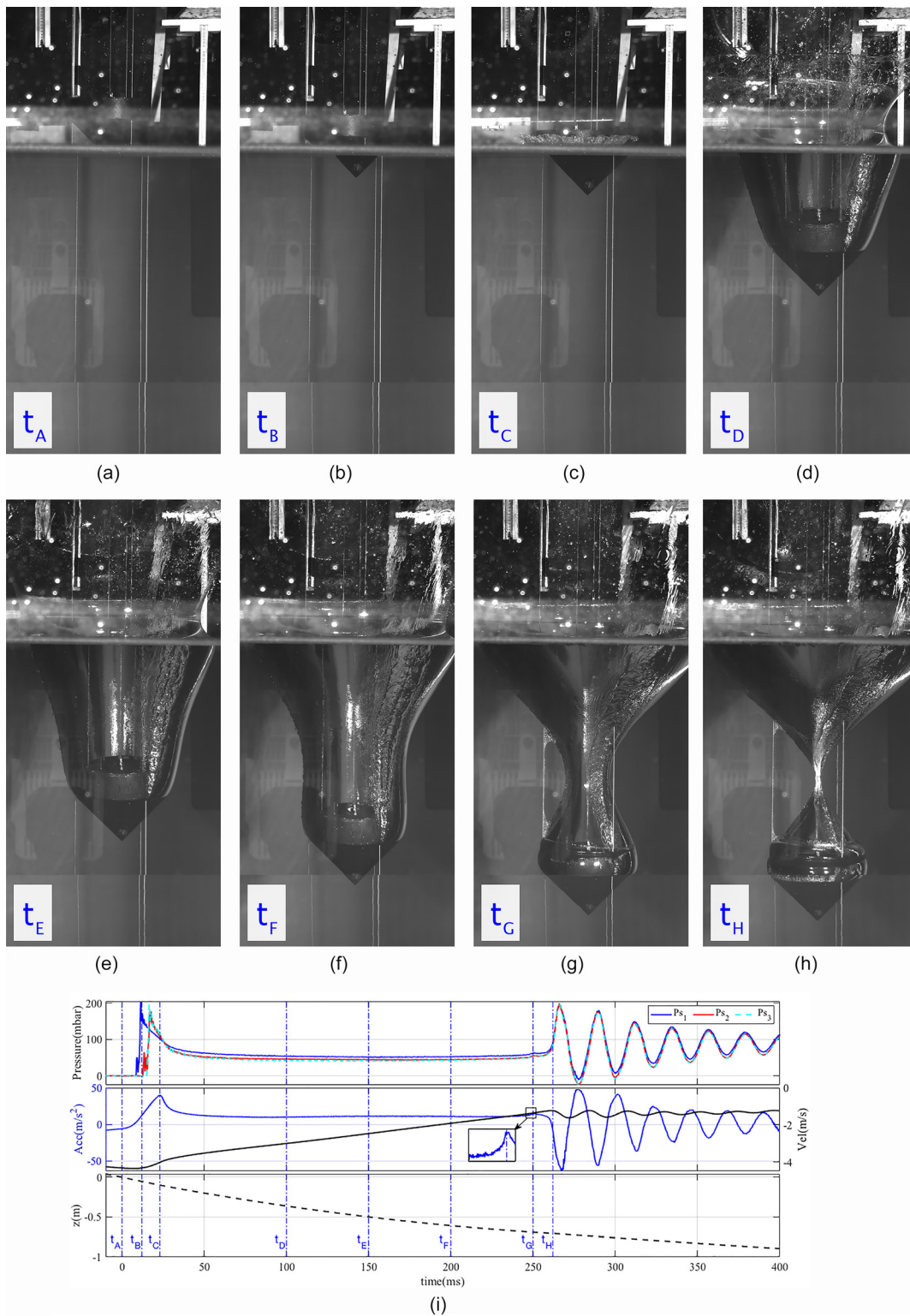
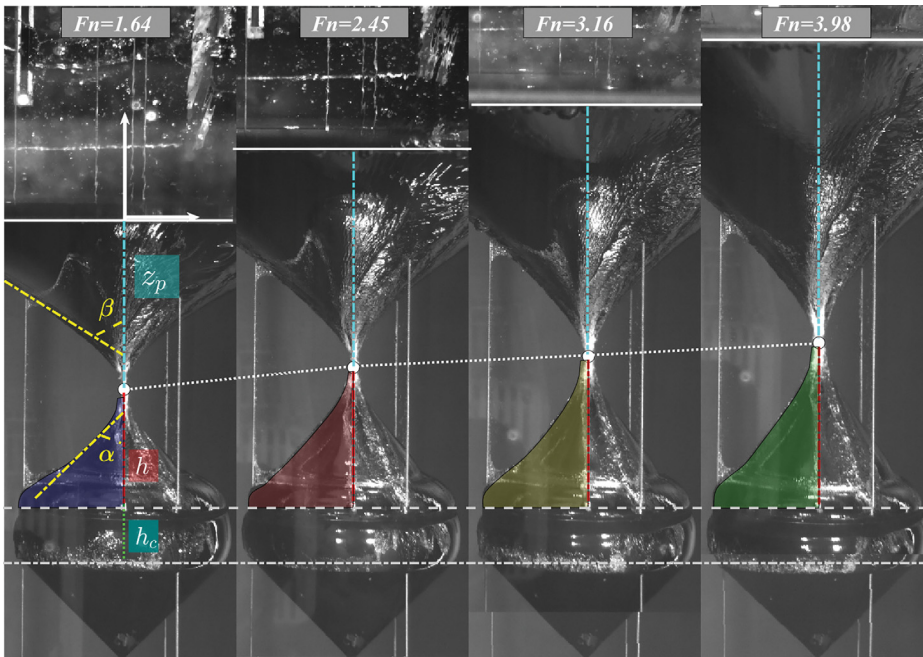


FIG. 4. Case  $p_u = p_{atm}$  and  $Fn = 3.98$ . Top panel: flow evolution of the body from the time instant  $t_A$  of the impact and until the pinch off of the cavity  $t_H$ . Bottom panel: time histories of the pressure probes on the body (first diagram), velocity and acceleration (second diagram), and vertical position (third diagram) of the body.





**FIG. 5.** Experimental images of the two cavities just before the closure time instant at different Froude numbers. The definition of the geometrical quantities is indicated: position of the pinch-off point (white circle); its distance from the undisturbed free-surface,  $z_p$  (cyan line); angle  $\beta$  of the open cavity; distance  $h$  between the pinch-off point and the center of the aft-body (red line); and angle  $\alpha$  of the closed air-cavity. Finally,  $h_c$  indicates the height of the cylindrical part of the body.

Because of the size of the body and the impact velocities realized in the present experiments, we get  $Re > 10^5$ ,  $We \gg 1$ , and  $Bo \gg 1$ ; the Froude number is the only nondimensional group governing the scaling of the geometrical and kinematic quantities until the deep closure of the cavity. The left panel of Fig. 6 shows the scaling with  $Fn$  of the distance from the free surface  $z_p$  of the pinch-off point and of the depth  $H(t_p) = z_p(t_p) + h(t_p) + h_c$  of the body at the pinch-off time. Note that the latter includes also the height  $h_c$  of the cylindrical part of the body; the flow separation from the body surface initially occurs indeed at the ends of the conical shape (Fig. 4). Both the quantities have been nondimensionalized with the radius of the cone, i.e.,  $z_{ad}$

$= z_p/c_0$  and  $\zeta_{ad} = H/c_0$ . According to the previous studies on the water entry problem of a sphere,<sup>18</sup> a linear scaling is confirmed. For  $Fn > 4$  and for  $D < 1.5$ , Aristoff *et al.*<sup>18</sup> assessed the influence of the mean acceleration (or deceleration) after the initial impact of the body on the scaling procedure. However, in the present experiments,  $D \approx 1.9$  and  $Fn < 4$ , so we did not take into account the acceleration contribution. Note that the ratio  $Z_{ad} = z_p/H$  (square symbols in Figure 6) remains almost constant with  $Fn$ , specifically  $Z_{ad} \approx 0.5$ ; a similar behavior was also observed in Aristoff *et al.*<sup>18</sup> for a sphere. An important kinematic quantity characterizing the closure of the cavity is the pinch-off time  $t_p$ , which is reported in the right panel of Fig. 6. In

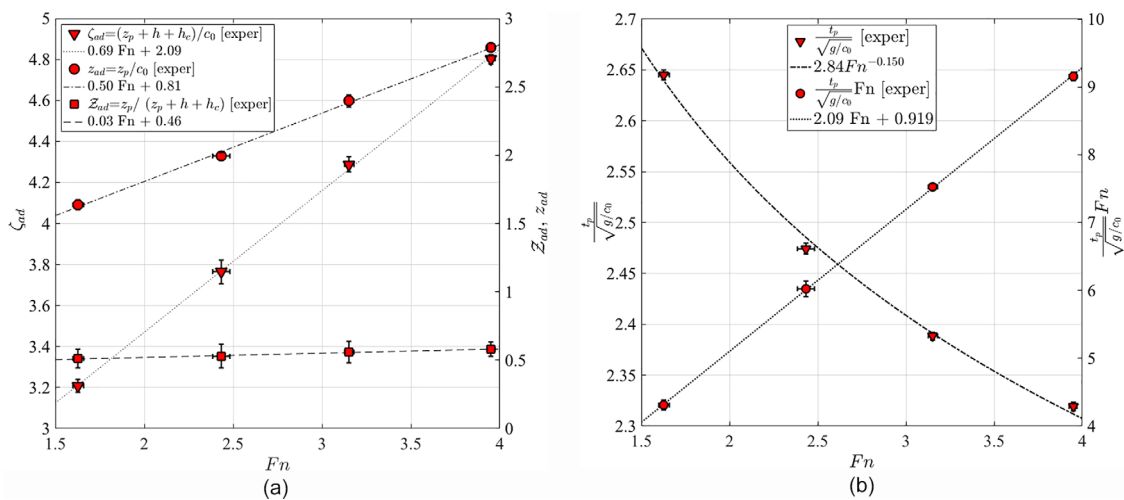


**FIG. 6.** Left panel: geometry of the cavity at the pinch off time as a function of the Froude number. Right panel: nondimensional pinch-off time vs Froude number. The lines represent the best fitting of the experimental data.

accordance with the results by Aristoff *et al.*,<sup>18</sup> the dominant term of the theoretical nondimensional quantity  $t_p/(c_0/U_0)$  linearly varies with  $Fn$  or  $t_p/\sqrt{c_0/g}$  is constant. This approximation was also observed by Gilbarg & Anderson<sup>9</sup> and Ducleaux *et al.*<sup>19</sup> Actually,  $t_p/\sqrt{c_0/g}$  can be weakly dependent on the Froude number  $Fn$  for the vertical water entry of solid objects.<sup>18,20</sup> In the present experiments, a proper scaling of the pinch-off time, i.e.,  $t_p/\sqrt{c_0/g}$ , is emphasized, at least for a free-falling cone within the relatively small range of  $Fn$  considered. It is found that  $t_p/\sqrt{c_0/g}$  is weakly dependent on  $Fn$ , namely,  $t_p/\sqrt{c_0/g}$  is proportional to  $Fn^{-0.15}$ .

To further inspect the geometrical scaling of the cavity at the closure time instant, the left panel of Fig. 7 shows the initial volume of the closed cavity, i.e., at  $t = t_p$ , calculated through Eq. (1) and nondimensionalized by the body volume  $\Delta_{tot}$ . In order to account for the real flow detachment, the quantity  $Vol + \Delta_{cyl}$ , which includes the volume of the cylindrical part of the body, is also reported in the same figure. Note that in this case, the quantity has been nondimensionalized with the volume of cone,  $\mathcal{V}_{ad} = (Vol + \Delta_{cyl})/\Delta_{cone}$ . For both the quantities, despite a quite large scattering of the measured data, related to the image identification procedure with possible distortion error, a quite clear linear scaling with  $Fn$  is observed. For a free-falling sphere,<sup>18</sup> the dimensionless volume of the closed cavity at  $t_p$  is strongly affected by the deceleration of the body after the impact stage, also for  $D > 1.5$ , causing the variation from a linear to a nonlinear trend, at least within the range  $2 < Fn < 4$ . However, the different body geometry used in the present case does not allow a straightforward use of the relationship proposed by Aristoff *et al.*<sup>18</sup> The slenderness of the open and closed cavities can provide useful information to define their shapes. The right panel of Fig. 7 shows the scaling of the angle featuring the closed (i.e.,  $\alpha$ ) and the open (i.e.,  $\beta$ ) cavity. Note that the angle here measured is the almost constant angle, which characterizes the cavity just after the rapid variation of its surface steepness at the pinch-off point (Fig. 5). Generally,  $\beta > \alpha$ , and both have a similar scaling  $\approx Fn^{1/4}$  with a difference that is almost constant (square symbols

in the right panel of Fig. 7) with  $Fn$ . More slender cavities, i.e., with lower angles  $\alpha$  and  $\beta$ , originate at larger  $Fn$ ; this is also a consequence of the increasing value of  $H(t_p)$  with  $Fn$ .<sup>21</sup>

A kinematic quantity to be monitored during the cavity closure is the radial velocity  $r_c$  of the air-water surface developing a neck of thickness  $2r_c$  (left panel of Fig. 8), which minimizes at the pinch-off point at  $t = t_p$ , ensuring the Worthington and downward jets (right panel of Fig. 8). This quantity was rarely measured, at least to our knowledge, in the water-entry experimental studies available in the literature, but it is a key parameter for the modeling of the evolution of the jets in the open and closed cavities.<sup>21</sup>

The time evolution of the radial velocity of the neck is shown in the right panel of Fig. 9 for different  $Fn$  values. First, a quite large radial acceleration of the flow just close to  $t_p$  is evident; this scenario will be the premise for the successive generation of a stagnation point from the closure of the neck, as it will be discussed in Sec. III B.

It is interesting to highlight the weak dependence on  $Fn$  ( $\approx Fn^{-0.15}$ ), which confirms the scaling of  $t_p$ .

The time evolution of the minimum radial distance  $r_c$  of the neck during the closing cavity process is shown in the left panel of Fig. 9 for different  $Fn$  values.

This quantity is fundamental in the comprehension of the physical mechanism underlying the bubble breakup.<sup>22</sup> In their study, Gordillo *et al.*<sup>22</sup> distinguished two different types of breakup mechanisms: (i) symmetric breakup, characterized by the formation of two symmetric bubbles after the pinch-off time instant; and (ii) asymmetric breakup, with the generation of two bubbles with different sizes. According to their outcomes,<sup>22</sup> two different scalings of  $r_c(\tau = t - t_p)$ , with  $\tau$  the time to breakup, exist within the limit of  $\tau \rightarrow 0$ . For the case of large  $Re$  and negligible surface tension effects, the scaling  $\tau^{1/3}$  is valid for the asymmetric breakup and  $\tau^{1/2}$  for the symmetric one. When surface tension matters, a scaling  $\tau^{2/3}$  must be expected. According to Gordillo *et al.*,<sup>22</sup> the transition to  $\tau^{1/3}$  happens for  $r_c \leq r_{trans}$  with  $r_{trans}/c_0 \approx \Lambda^{1/2} Q_a/q(\tau)$ . Here,  $\Lambda$  is the density ratio between inner (air) and outer (water) flows,  $Q_a$  is the non-

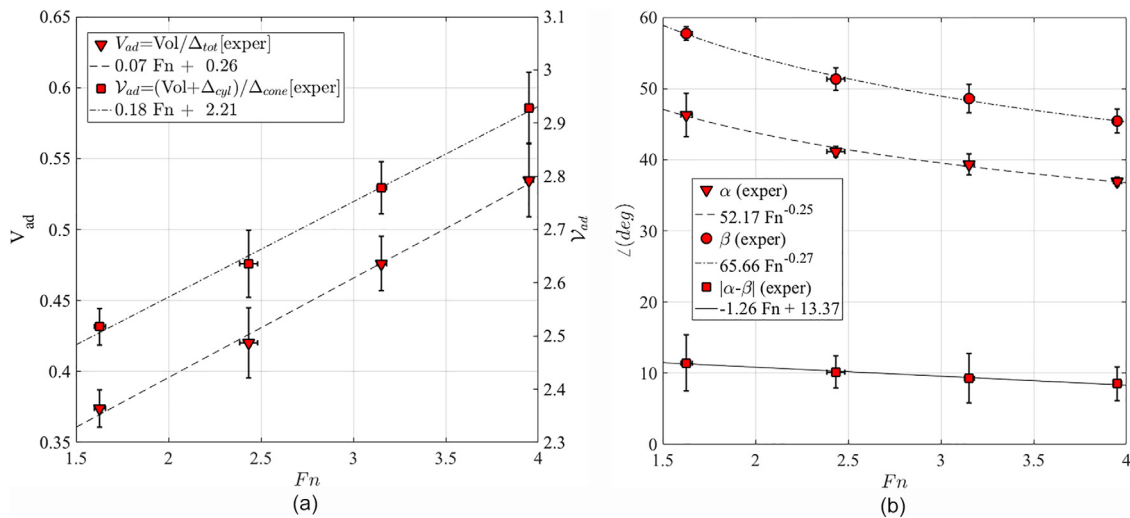
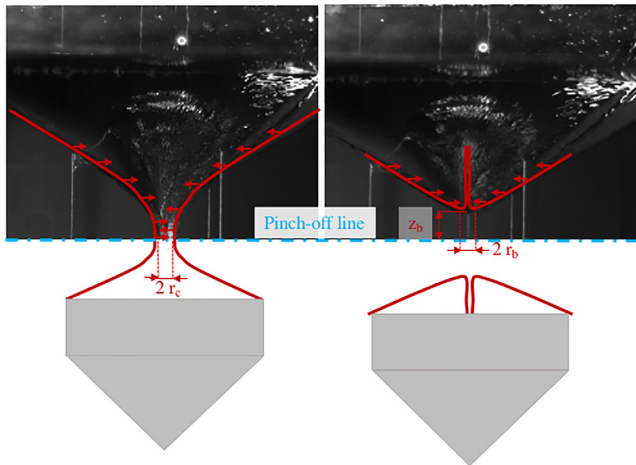


FIG. 7. Left panel: volume of the closed cavity at the pinch off time as a function of the Froude number. Right panel: angle of the closed ( $\alpha$ ) and open ( $\beta$ ) cavities vs Froude number. The lines represent the best fitting of the experimental data.



**FIG. 8.** Left panel: definition of the neck (minimum distance of the free surface) during the cavity closure process. Right panel: definition of base for the Worthington jet. The same quantities can be defined for the downward jet.

dimensional air flow rate, and  $q(\tau) = \dot{r}_c r_c / (U_0 c_0)$ . The cavity closure process around the pinch-off time resembles the asymmetric bubble breakup with the formation of a closed cavity (small bubble) attached to the body and an open cavity (large bubble) on the upper part. It is, then, relevant to check the scaling of  $r_c$  with the time to pinch-off. From the experiments, we have estimated a characteristic radius of  $r_{trans}/c_0 \approx 0.15 - 0.2$ , which allows us to assess a scaling of  $r_c$  with  $\tau^{1/3}$  as evident in Fig. 10. In the same figure, the 1/2 and 2/3 power laws are also reported, which confirm that the final stage of the pinch-off is governed by air and liquid inertia. This conclusion is further corroborated by the time evolution of the pressure measured on the top of the body and reported in the bottom panel of Fig. 11; the pressure in the cavity, indeed, increases before the pinch-off time, occurring slightly after  $t_H$ .

**B. Flow evolution after the closure of the cavity**

To describe this stage of the flow evolution, we refer to Fig. 11, i.e., the same experimental test considered in Fig. 4 ( $p_u = p_{atm}$  and  $Fn = 3.98$ ) but with a special care to the time evolution after the

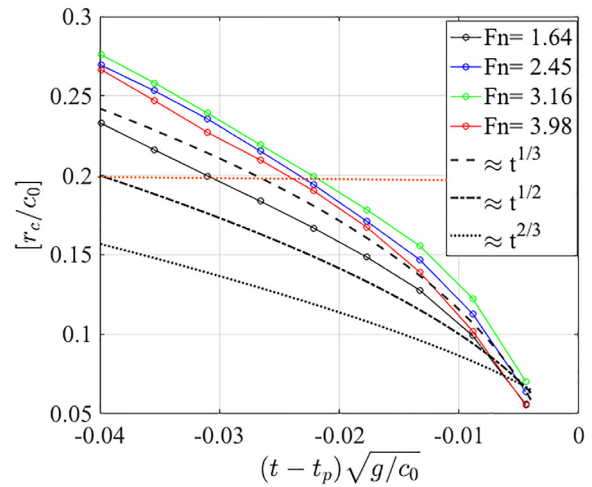


**FIG. 10.** Enlarged view of the time evolution of the nondimensional radial distance near the pinch-off time.

pinch-off, i.e.,  $t \geq t_H$ . Here, in the bottom panel, the vertical trajectory of the body is substituted by the pressure measured through four transducers (from  $Pt_1$  to  $Pt_4$ ) placed on the top of the body, that is, within the gas cavity.

After the pinch-off, a new scenario appears: a closed oscillating cavity is generated behind the body and remains attached to it, while an open cavity limited by the original free surface rebounds back and moves upward as a deformable inverted bell (Fig. 11). Because of the opposite evolution direction of the two cavities, their mutual influence is expected to quickly vanish, e.g., at  $t = t_b$ , the distance between the peaks of the two cavities is already larger than the body diameter.

At the pinch-off time  $t \approx t_H$ , two distinct jets born at the point of the cavity closure:<sup>4</sup> the Worthington jet, which moves up vertically toward the initial surface, and the downward jet, which evolves within the cavity. Both of them are well visible in Fig. 11 starting from the time instant  $t_f$ . Gilbarg and Anderson<sup>9</sup> have highlighted that they are the physical consequences of the large pressure gradient in the vertical direction occurring at the point of the initial cavity closure. In the presence of a free boundary, the formation of an upward and a downward

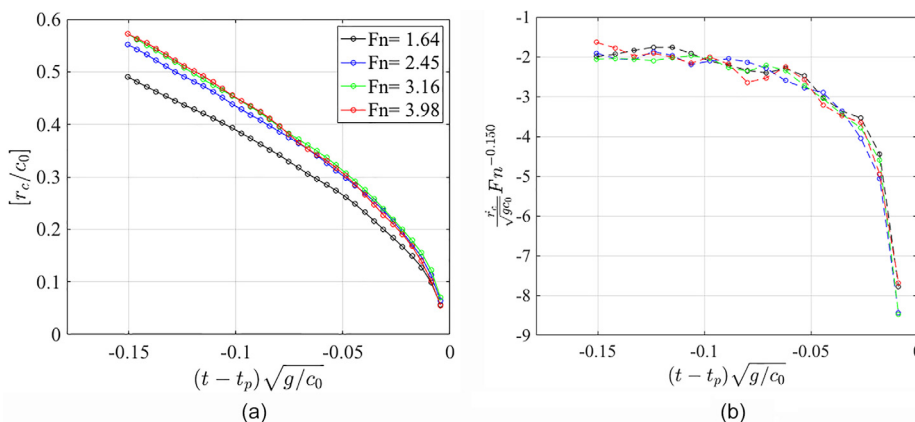


**FIG. 9.** Time histories of the minimum radial distance (left panel) and of the radial velocity (right panel) of the neck (shown in the left panel of Fig. 8) during the cavity closure process.

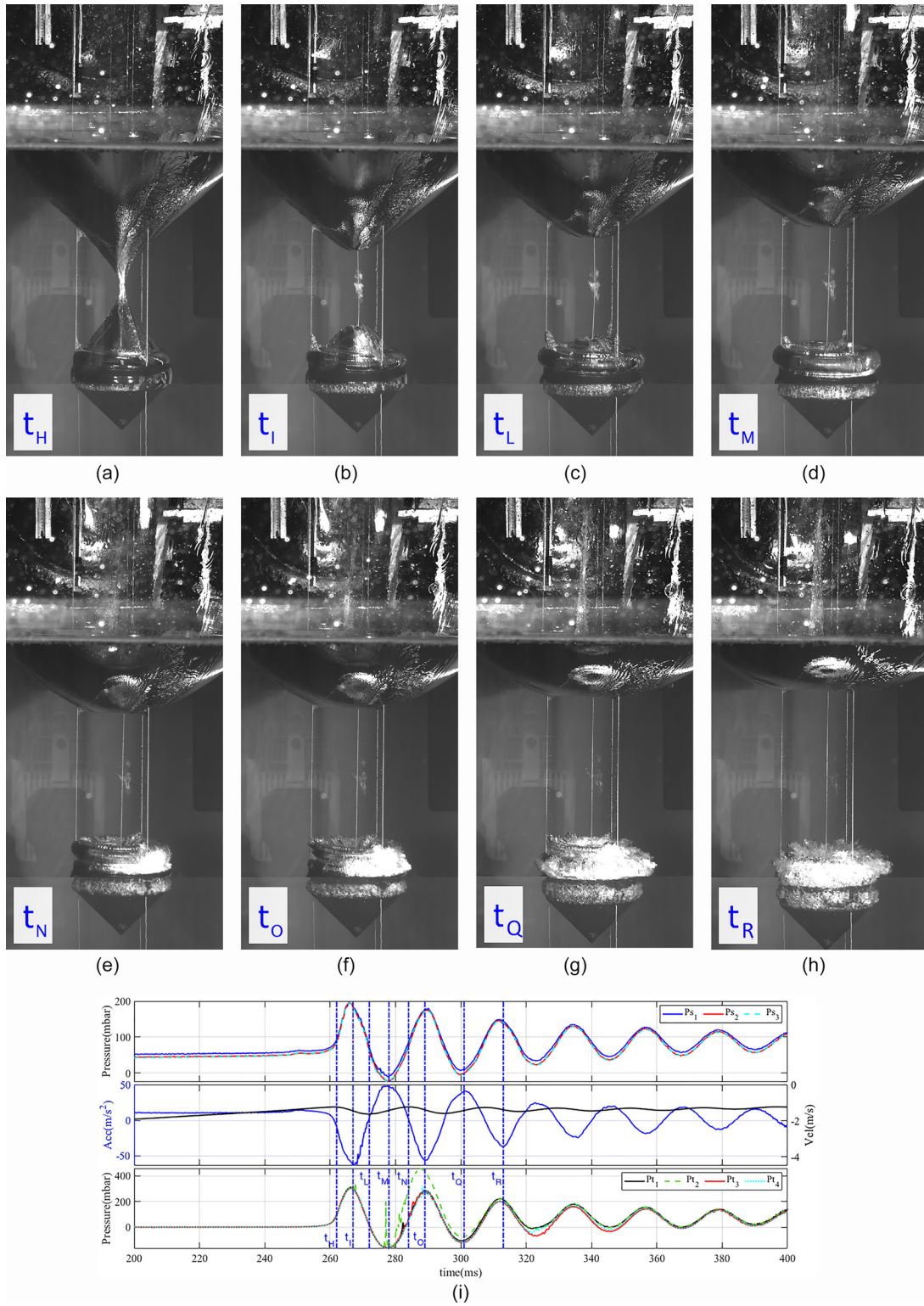


FIG. 11. Case  $\rho_u = \rho_{atm}$  and  $Fn = 3.98$ . Top panel: flow evolution of the body from the time instant  $t_H$  just before the pinch off of the cavity. Bottom panel: time histories of the pressure probes on the body (first diagram), velocity and acceleration (second diagram), and pressure on the top of the body (third diagram).

jet becomes, then, a physical need. This phenomenon evokes the physical observation by Lugni *et al.*<sup>14,23</sup> for the impact of a plunging wave against a vertical wall. Despite the 2D flow there reproduced, a similar vertical splitting of the horizontal mass of water impacting the wall is observed in Fig. 3 of Lugni *et al.*<sup>23</sup> as a consequence of the stagnation point occurring within the impact area: the vertical wall is a symmetry plane for the 2D impinging wave. In the present investigation, a symmetry axis of the 3D problem exists, but no symmetry wall is present. A clear picture of the flow evolution after the cavity closure has been provided by Geckle and Gordillo<sup>21</sup> for a circular disk impacting a still water surface at constant velocity: after the cavity collapse, the radial deceleration of the liquid at the jet base develops a stagnation point with a strong overpressure, which deflects the flow in the axial direction, both upward and downward. In this physical mechanism, the axial pressure gradient is generated continuously, while the cavity collapses; this is a further crucial difference with respect to the impact of a wave against a vertical wall mentioned above,<sup>23</sup> where the axial gradient exists at a well-defined and extremely short time interval, practically coinciding with the impact time. In their description of the jet structure, generally valid for both the Worthington and downward jets, Geckle and Gordillo<sup>21</sup> defined two main regions in which the flow around the jet is split, identified by the jet base, placed at a radial

distance  $r_b$  from the jet tip (i.e.,  $2r_b$  is a measure of the jet width) and at a vertical distance  $z_b$  from the pinch-off plane: an outer region for  $r > r_b$  and  $z < z_b$  and a jet region for  $r < r_b$  and  $z > z_b$  (Fig. 8).

In the latter, the jet evolution characterized by three spatial subregions, from the jet base where the flow is radially decelerated and axially accelerated (*acceleration region*) up to the *tip region* where the jet disrupts into the drops, takes place. In our experimental results, the measurement of the radial and axial positions of the jet base, i.e.,  $r_b$  and  $z_b$ , reported in the left column of the Fig. 12 for the Worthington jet and in the right column for the downward jet, respectively, is crucial for characterizing the behavior of both the jet flows, during the first time instants after the closure. Since the cavity is completely closed, a role of the air compressibility within the closed cavity, i.e., through the Euler number, is expected. This motivates the legends of Fig. 12, which report both the  $Fn$  and  $Eu$  numbers. It is crucial to note that the dynamic pressure used to define the  $Eu$  number is based on the impact velocity  $V_0$ . This means that the cases analyzed in the top panels of Fig. 12 refer to a constant value of the ambient pressure, namely, atmospheric pressure. In contrast, the  $Eu$  values reported in the bottom panels of the same figures are relative to almost constant  $Fn$  but to different values of the ambient pressure, approximately equal to 1 bar, 500 mbar, 250 mbar, 125 mbar, and finally 42 mbar. The time

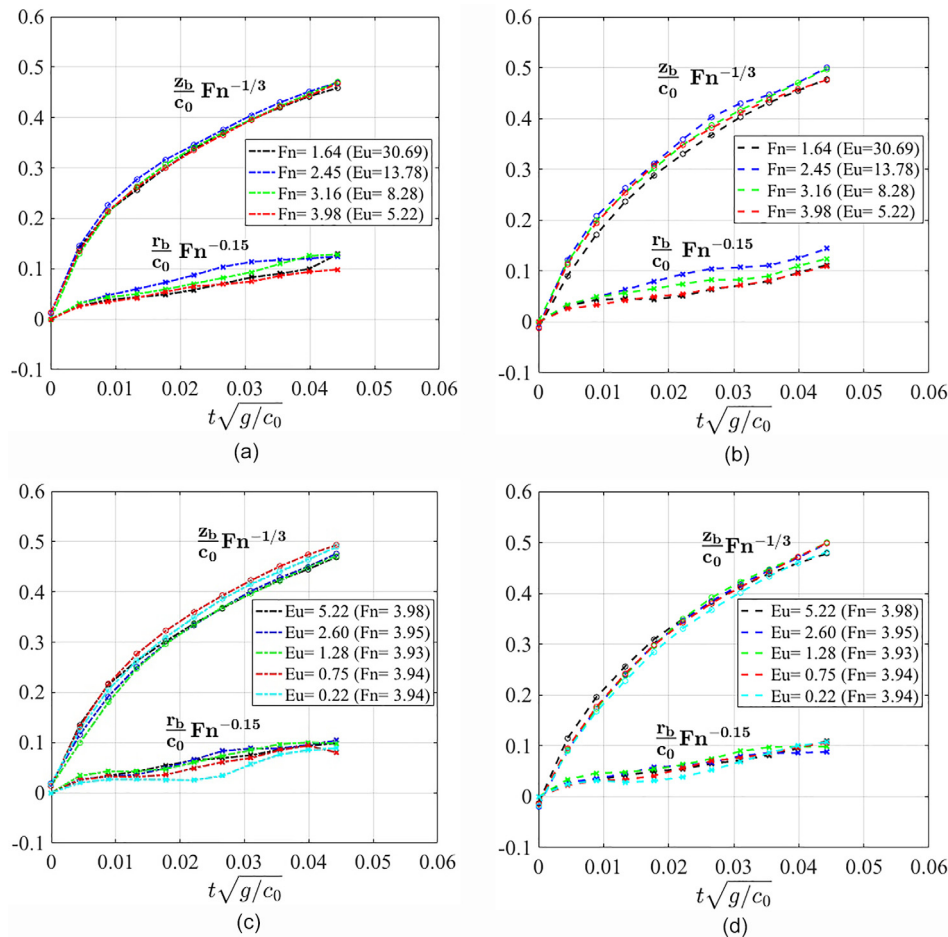


FIG. 12. Time evolution of the Worthington (left column) and downward (right column) jet base at  $p_u = p_{atm}$  and for several  $Fn$  (top panels) and at  $Fn$  almost constant but different  $p_u$  and then different  $Eu$  (bottom panels).

evolution of the radial and axial positions of the jet base follows the nonlinear behavior reported in Geckle and Gordillo.<sup>21</sup> However, with the aim to point out the scaling with the  $Fn$  and  $Eu$  numbers, the reference time  $\sqrt{c_0/g}$  is here used instead of  $c_0/U_0$  used by Geckle and Gordillo.<sup>21</sup> In this way, a well specific trend as  $Fn^{1/3}$  has been assessed for  $z_b$ . In contrast, the radial position follows the same weak dependence on  $Fn$  observed by the neck of the cavity before the closure. It is, however, relevant to remark that (i) the dynamics of the downward jet base, both in terms of  $z_b$  and  $r_b$ , is completely independent of  $Eu$ ; (ii) both the Worthington and downward jet bases show a really similar behavior, meaning that the flow splitting, i.e., upward and downward, at the stagnation point, is completely symmetric. These aspects matter for the jet dynamics.

The downward jet can be relevant for the body dynamics;<sup>4</sup> its evolution leads to an impact on the center of the top part of the body with a possible influence on the body acceleration and on its trajectory. The entity of the force impulse, estimated as  $0.5\pi\rho_w U_j r_b^3$ , with  $\rho_w$  the water density and  $U_j$  the impact velocity, provides a velocity contribution negligible in the present case because of the small radius of the jet (with respect to the size of the body, i.e.,  $r_b/c_0 \ll 1$ ) and the short duration of the jet interaction with the top of the body (Fig. 11). However, this contribution can be significant for smaller and faster bodies, as for the projectiles.

The measurement of the time evolution of the pressure within the cavity (bottom panel of Fig. 11) along with the synchronized images of the cavity evolution (Fig. 11) enables some insights into the flow evolution of the downward jet:

- at first glance, the pressure measured by the transducers on the top of the body is almost constant in space, except for the transducer  $P_{t_2}$  (green line in Fig. 11);
- the pressure transducer  $P_{t_2}$  is located at 20 mm from the center of the cone (refer to Methods for the detailed description of the setup), i.e., it is the closest to the axis of symmetry of the cone.
- $P_{t_2}$  shows an impulsive peak slightly before  $t = t_M$ , followed by a pressure variation in the successive oscillation period of the cavity. Because of the symmetry of the problem, the maximum pressure peak is expected at the center of the cone. However, the setup used enables us to guess that the pressure peak in  $P_{t_2}$  is

caused by a deviation of the jet flow from the center of the cone, which impacts the pressure probe  $P_{t_2}$ . The local water level accumulation induced by the continuous water intake of the jet flow causes an increase in the ensuing pressure until the collapse of the bubble at  $t = t_Q$  (green line from  $t = t_M$  up to  $t = t_Q$  in Fig. 11). This interpretation has been further validated through a simple test in the laboratory, by generating a water jet flow, through a water hose, impacting the hat of the cone.

The load in the closed cavity can be, then, considered spatially constant and variable in time as a consequence of the free oscillation of the cavity at its own resonance frequency. The maximum amplitude of the pressure load at the first peak and the eigenfrequency of the cavity are two fundamental parameters for the correct design of a body during the water-entry problem: the first one for checking the maximum structural load and the second one to prevent possible hydroelastic issues.<sup>24</sup> It is, then, crucial to assess the correct scaling of these two physical quantities for a proper evaluation on prototype when only scaled model test data are available. According to Faltinsen and Timokha,<sup>25</sup> the eigenfrequency of a closed gas cavity depends on the volume and on the gas pressure within the cavity at the closure time and on the velocity field around: the Euler number and the Froude number matter for the scaling of both the frequency and the maximum load within the cavity, i.e., the interaction between body and cavity dynamics is important. For the first time, the present experimental study faces this issue on the water-entry problem of a 3D axisymmetric body; the main results are reported in Figs. 13 and 14.

The left panels, reporting the error bar of the frequency (Fig. 13) and of the pressure load (Fig. 14), allow us to separate the effect of  $Fn$  from  $Eu$ . Note that the error bar accounts for the values measured in each test by the four pressure transducers on the top of the body, i.e., within the cavity. Once  $Fn$  scaling has been determined, an iterative procedure is used to properly determine the  $Eu$  dependency, whose results are reported in the right panel of the same figures. First, the oscillation frequency of the bubble scales with  $Fn^{0.76} Eu^{0.46}$ , with the  $Eu$  scaling being quite similar to the theoretical results achieved by Faltinsen and Timokha<sup>25</sup> for a 2D cavity. The maximum pressure in the cavity, and then the maximum load, i.e., the pressure is spatially constant in the cavity, presents an interesting scaling as  $Fn^{1.9} Eu^{0.59}$ .

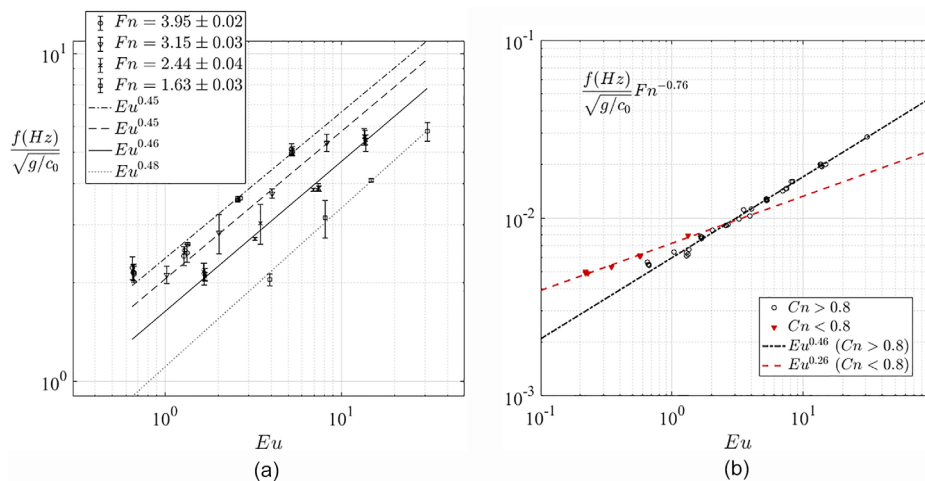


FIG. 13. Scaling behavior of the oscillation frequency of the cavity.

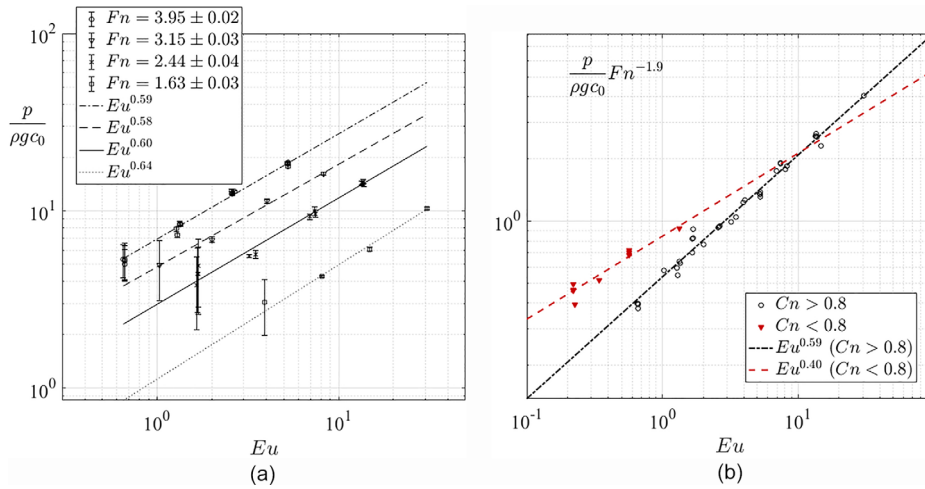


FIG. 14. Scaling behavior of the maximum pressure at the first oscillation peak of the cavity.

This means that the  $Fn$  scaling is really similar to the one valid for the peak pressure during the first impact of the body on the still water; however, in this case, a nonnegligible effect comes from the  $Eu$  scaling, confirming the mutual role of the body and cavity dynamics. All the data presented in Figs. 13 and 14 and colored by the black symbols refer to the cases with cavitation number  $Cn > 0.8$ , for which we can assess that cavitation phenomena do not occur. In the definition of  $Cn$ , we have assumed  $p_v = 3600Pa$ , which corresponds to a temperature between  $25^\circ C$  and  $30^\circ C$ , i.e., the range of temperatures measured during the tests. Note that the right panel of both Figs. 13 and 14 does not report any error bar. This choice is motivated by the low number of repeated tests at the same condition. So, in this case, we have chosen to report all the results of different runs separately.

For the practical design, it is highly relevant to observe that for the cases with  $Cn < 0.8$  (red symbols in the right panels of Figs. 13 and 14), the  $Eu$  scaling is substantially different, both for the frequency and the maximum load. This means that, in the presence of cavitation phenomena, the influence of  $Cn$  must be taken into account.

The strategy used to identify the scaling process, both before the pinch-off time instant, when  $Fn$  dominates, and after the cavity

closure, when both  $Fn$  and  $Eu$  matter, is based essentially on the identification of some local and specific quantities, e.g., maximum pressure load, pinch-off time, and oscillation frequency of the bubble. It is, however, interesting to understand how much the scaling can be extended to the evolution of the whole process. For this purpose, Fig. 15 shows the whole evolution of one of the pressure transducers placed along the cone surface (left panel) and on the top of the cone, i.e., within the cavity (right panel) for nine different cases reported in the legend of the figure. Each panel reports the scaling of the time and of the loads assessed in the present study; the dot-dashed line represents the pinch-off time instant, which separates the  $Fn$  scaling typical of the time evolution until the closure (i.e.,  $t < t_p$ ) from the  $Fn$  and  $Eu$  scalings (by assuming  $Cn \approx > 1$ ), which characterize the load evolution after the cavity closure, i.e., for  $t > t_p$ . Note that in the first region, the scaling used ( $\approx Fn^{-2}$ ) works well for the maximum pressure peaks at the impact time instant, but it cannot work, as expected, for the load scaling during the following evolution (until the cavity closure) where the gravity-term loads dominate.<sup>10</sup> However, here we focus on the second region, i.e.,  $t > t_p$ , since the first one was well studied in the literature.<sup>18</sup> In the following, the loads for  $t > t_p$  have been purged of the

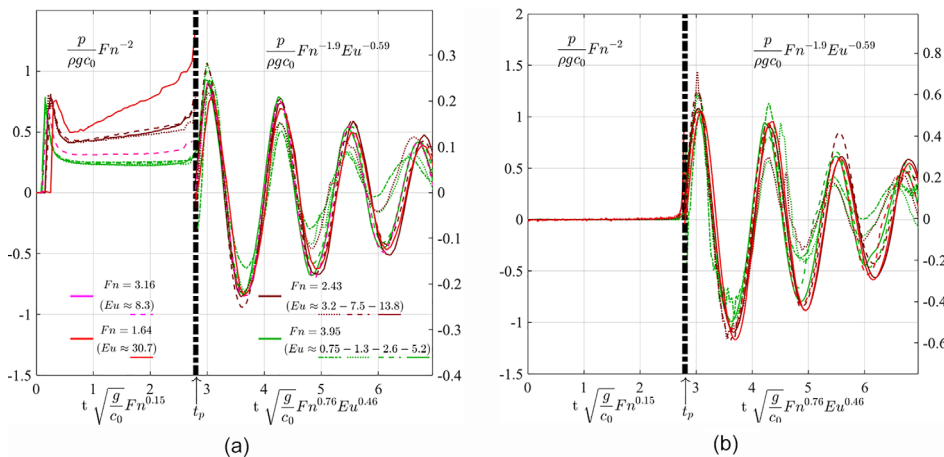


FIG. 15. Scaling of the pressure in time along the body (left panel) and within the cavity (right panel).

mean value. Generally, the whole time history of the local load in the cavity, as well as of the induced compressibility load induced on the cone, scales well with  $Fn^{1.9}Eu^{0.59}$  and the frequency with  $Fn^{0.76}Eu^{0.45}$ , at least for  $Eu \approx 5$ . In contrast, for  $Eu < 5$ , we observe that after the first oscillation, the nonlinear pressure-density relationship characterizing the air-cavity dynamics matters and modifies the scaling process of the pressure evolution. This outcome, by corroborating previous experimental findings by Lugni *et al.*,<sup>14,23</sup> on the impact flow of a 2D wave against a vertical wall with the air cavity entrapped, supports the conclusion that loads on full scale might be more nonlinear than on model scale.<sup>25</sup>

#### IV. CONCLUSION

Our present investigation opens a new frontier on the hydro-structural design of a free-falling conical body shape entering the still water surface at relatively low impacting speeds and entrapping an air cavity. Most of the available literature focuses on the stage preceding the closure of the cavity, for different shapes of the body (typically sphere and conical shape as projectiles) and quite large  $Fn$ . Our results confirm some previous studies:

- (1) in accordance with Aristoff *et al.*,<sup>18</sup> both the position of the pinch-off point behind a sphere, i.e., its distance from the initial undisturbed free surface, and the depth of the body at the pinch-off time linearly depend on  $Fn$ ;
- (2) the experimental findings confirmed a linear variation of the nondimensional pinch-off time  $t_p/(c_0/U_0)$  with respect to  $Fn$ , as found by Ducleaux *et al.*<sup>19</sup> and Aristoff *et al.*<sup>18</sup> However, for the first time, our analysis confirmed that  $t_p/\sqrt{c_0/g}$  is weakly dependent on  $Fn$ , that is, as  $Fn^{-0.15}$ ;
- (3) the cavity-closure process around the pinch-off time resembles the asymmetric bubble breakup with the formation of a closed cavity (small bubble) attached to the body and an open cavity (large bubble) on the upper part. The scaling of the neck thickness  $r_c$  with the time to pinch-off  $\tau$  confirms a scaling with  $\tau^{1/3}$ , as already assessed by Gordillo *et al.*<sup>22</sup> when the surface tension effect is negligible and the air and liquid inertia dominate.

The contribution given to the stage after the closure of the cavity is even more relevant. This stage is characterized by the cavity oscillations and by a relevant effect of the air compressibility, which provides the restoring contributions. The cavity natural frequency scales  $\approx Fn^{0.76}Eu^{0.46}$ ; the  $Eu$  scaling resembles the previous findings for the oscillation of the cavity entrapped in the wave-impact problem.<sup>14,25</sup> For the first time, the experimental scaling of the maximum loads occurring on the body and induced by the cavity oscillation has been assessed, emphasizing the mutual role of the  $Fn$  and  $Eu$  numbers. A scaling that  $Fn^{-1.9}Eu^{-0.59}$  has been found for the maximum pressure in the cavity. However, it is crucial to avoid the cavitation phenomena on model scale; since they do not occur on the prototype for the case of our interest, their occurrence in the model tests can modify the scaling and the physical evolution of the flow field. This is relevant for a proper choice of the scale factor for the model test applications.

Our results refer to a well specific body shape and a well specific mass ratio; they suggest new similar studies for a full comprehension of the universality of the scaling law. However, the availability of such an experimental analysis enables a proper validation of the numerical models that can be, then, used for more general studies.

#### ACKNOWLEDGMENTS

This work was supported by the Ministry of Science and Technology of P. R. China through Harbin Engineering University (No. G20190008061) and the National Natural Science Foundation of China (No. 51509028). C.L. and O.M.F. were also supported by the Research Council of Norway through the Centers of Excellence funding scheme AMOS, Project No. 223254. A.B. thanks the Italian Ministry of University and Research (MUR) for supporting the research through the A.I.M. (Attrazione e Mobilità Internazionale) project, within the National Operational Programme for Research and Innovation (PON R&I 2014–2020). C.L., A.B., and A.L. also acknowledge the Italian Ministry of Economic Development (MiSE) for the support under the Grant Agreement RdS PTR 2019–2021-Tema 1.8: Energia elettrica dal mare. For C.L. this study was partly carried out in the framework of the project ARES (PON Ricerca e Innovazione 2014-2020, project code: ARS01-00682-V0086), co-funded by the European Union.

The authors declare no competing interest.

#### DATA AVAILABILITY

The data that support the findings of this study are available from the corresponding author upon reasonable request.

#### REFERENCES

- <sup>1</sup>O. Faltinsen, "The effect of hydroelasticity on ship slamming," *Philos. Trans. R. Soc. A* **355**, 1–17 (1997).
- <sup>2</sup>J. Wang, C. Lugni, and O. M. Faltinsen, "Analysis of loads, motions and cavity dynamics during freefall wedges vertically entering the water surface," *Appl. Ocean Res.* **51**, 38–53 (2015).
- <sup>3</sup>J. Wang, C. Lugni, and O. M. Faltinsen, "Experimental and numerical investigation of a freefall wedge vertically entering the water surface," *Appl. Ocean Res.* **51**, 181–203 (2015).
- <sup>4</sup>T. Truscott, B. Epps, and J. Belden, "Water entry of projectiles," *Annu. Rev. Fluid Mech.* **46**, 355–378 (2014).
- <sup>5</sup>A. May, "Vertical entry of missiles into water," *J. Appl. Phys.* **23**, 1362–1372 (1952).
- <sup>6</sup>H. S. Alsos and O. M. Faltinsen, "3D motion dynamics of axisymmetric bodies falling through water," *Ocean Eng.* **169**, 442–456 (2018).
- <sup>7</sup>R. Hurd, J. Belden, A. Bower, S. Holekamp, M. Jandron, and T. Truscott, "Water walking as a new mode of free surface skipping," *Sci. Rep.* **9**, 6042 (2019).
- <sup>8</sup>J. Aristoff and J. Bush, "Water entry of small hydrophobic spheres," *J. Fluid Mech.* **619**, 45–78 (2009).
- <sup>9</sup>D. Gilbarg and R. A. Anderson, "Influence of atmospheric pressure on the phenomena accompanying the entry of spheres into water," *J. Appl. Phys.* **19**, 127–139 (1948).
- <sup>10</sup>J. Wang, O. Faltinsen, and C. Lugni, "Unsteady hydrodynamic forces of solid objects vertically entering the water surface," *Phys. Fluids* **31**, 027101 (2019).
- <sup>11</sup>O. Faltinsen, *Sea Loads on Ships and Offshore Structures* (Cambridge University Press, 1990).
- <sup>12</sup>A. Korobkin and D. Peregrine, "The energy distribution resulting from an impact on a floating body," *J. Fluid Mech.* **417**, 157–181 (2000).
- <sup>13</sup>C. Devin, "Survey of thermal, radiation, and viscous damping of pulsating air bubbles in water," *J. Acoust. Soc. Am.* **31**, 1654–1667 (1959).
- <sup>14</sup>C. Lugni, M. Brocchini, and O. Faltinsen, "Evolution of the air cavity during a depressurized wave impact. II. The dynamic field," *Phys. Fluids* **22**, 056102 (2010).
- <sup>15</sup>A. Korobkin and V. Pukhnachov, "Initial stage of water impact," *Annu. Rev. Fluid Mech.* **20**, 159–185 (1988).
- <sup>16</sup>T. Truscott and A. Techet, "A spin on cavity formation during water entry of hydrophobic and hydrophilic spheres," *Phys. Fluids* **21**, 121703 (2009).
- <sup>17</sup>M. Perlin and S. Ceccio, *Mitigation of Hydrodynamic Resistance: Methods to Reduce Hydrodynamic Drag* (World Scientific, 2014), pp. 1–164.



- <sup>18</sup>J. Aristoff, T. Truscott, A. Techet, and J. Bush, “The water entry of decelerating spheres,” *Phys. Fluids* **22**, 032102 (2010).
- <sup>19</sup>V. Duclaux, F. Caillé, C. Duez, C. Ybert, L. Bocquet, and C. Clanet, “Dynamics of transient cavities,” *J. Fluid Mech.* **591**, 1–19 (2007).
- <sup>20</sup>J. Wang and O. Faltinsen, “Numerical investigation for air cavity formation during the high-speed water entry of wedges,” *J. Offshore Mech. Arct. Eng.* **135**, 011101 (2013).
- <sup>21</sup>S. Geckle and J. Gordillo, “Generation and breakup of Worthington jets after cavity collapse. Part 1. Jet formation,” *J. Fluid Mech.* **663**, 293–330 (2010).
- <sup>22</sup>J. Gordillo, A. Sevilla, J. R. Rodriguez, and C. M. Bazan, “Axisymmetric bubble pinch-off at high Reynolds numbers,” *Phys. Rev. Lett.* **95**, 194501 (2005).
- <sup>23</sup>C. Lugni, M. Miozzi, M. Brocchini, and O. Faltinsen, “Evolution of the air cavity during a depressurized wave impact. I. The kinematic flow field,” *Phys. Fluids* **22**, 056101 (2010).
- <sup>24</sup>C. Lugni, A. Bardazzi, O. Faltinsen, and G. Graziani, “Hydroelastic slamming response in the evolution of a flip-through event during shallow-liquid sloshing,” *Phys. Fluids* **26**, 032108 (2014).
- <sup>25</sup>O. Faltinsen and A. Timokha, *Sloshing* (Cambridge University Press, 2009).